Rapid Surface Oxidation as a Source of Surface Degradation Factor for Bi_2Se_3

Desheng Kong,[†,⊥] Judy J. Cha,[†,⊥] Keji Lai,[‡,§] Hailin Peng,[†,∥] James G. Analytis,[‡,#] Stefan Meister,[†] Yulin Chen,[‡,§,#] Hai-Jun Zhang,[§] Ian R. Fisher,[‡,#] Zhi-Xun Shen,[‡,§,#] and Yi Cui[†,*]

[†]Department of Materials Science and Engineering, Stanford University, Stanford, California 94305, United States , [‡]Department of Applied Physics, Stanford University, Stanford, California 94305, United States , [§]Department of Physics, Stanford University, Stanford, California 94305, United States, and [#]Stanford Institute for Materials and Energy Sciences, SLAC National Accelerator Laboratory, 2575 Sand Hill Road, Menlo Park, California 94025, United States. [∥]Present address: College of Chemistry and Molecular Engineering, Peking University, Beijing 100871, P. R. China. [⊥]These authors contributed equally to this work.

ABSTRACT Bismuth selenide (Bi_2Se_3) is a topological insulator with metallic surface states (SS) residing in a large bulk bandgap. In experiments, synthesized Bi_2Se_3 is often heavily n-type doped due to selenium vacancies. Furthermore, it is discovered from experiments on bulk single crystals that Bi_2Se_3 gets additional n-type doping after exposure to the atmosphere, thereby reducing the relative contribution of SS in total conductivity. In this article, transport measurements on Bi_2Se_3 nanoribbons provide additional evidence of such environmental doping process. Systematic surface composition analyses by X-ray photoelectron spectroscopy reveal fast formation and continuous growth of native oxide on Bi_2Se_3 under ambient conditions. In addition to n-type doping at the surface, such surface oxidation is likely the material origin of the degradation of topological SS. Appropriate surface passivation or encapsulation may be required to probe topological SS of Bi_2Se_3 by transport measurements.

KEYWORDS: topological insulator · nanoribbon · transport · oxidation · doping · bismuth selenide

Topological insulators (TIs) represent band insulators with helically spin-polarized metallic states on the surface.[1−3] Such surface states (SS), protected by time reversal symmetry, are of fundamental research interest and attractive for applications, such as in spintronics and quantum computing. Among the candidate materials,[4−12] layer-structured Bi_2Se_3 is an excellent TI with a single Dirac cone residing inside a large bandgap (~300 meV).[6,7] SS of Bi_2Se_3 have been extensively studied by surface-sensitive techniques such as angle-resolved photoemission spectroscopy (ARPES).[7,13−16] Recently, several transport experiments also revealed SS: Aharonov−Bohm oscillations arising from the interference of the TI SS, observed in tin (Sn)-doped Bi_2Se_3 nanoribbons;[17] Shubnikov−de Haas (SdH) oscillations of the SS in bulk single-crystal Bi_2Se_3, with pulsed, high magnetic fields up to 55 T;[18] and SdH oscillations of SS in gated thin flakes of Bi_2Se_3 mechanically exfoliated from bulk single crystals.[19] Despite these reports, many challenges still remain for studying SS by transport. For example, air exposure is shown as an n-type doping process for Bi_2Se_3,[20] consequently decreasing the contribution of the topological SS. For pulsed, high magnetic field measurements, SdH oscillations from topological SS are smeared out after 1 to 2 h of air exposure, direct evidence of the degradation of surface transport properties.[18] These experimental challenges question the idealized structure and composition of the surface of Bi_2Se_3, which appears to be modified by chemical reactions under ambient conditions. In the present work, systematic transport measurements on Bi_2Se_3 nanoribbons, combined with surface composition analyses, provide additional evidence for environmental doping. Based on X-ray photoelectron spectroscopy (XPS) characterizations, we show native oxide growth on Bi_2Se_3, both for nanoribbons and bulk crystals, which we surmise as the likely material origin of surface degradation and environmental doping. Possible mechanisms for the surface oxidation induced doping are discussed.

Transport measurements on Bi_2Se_3 nanoribbons provide additional evidence for n-type doping by air exposure. Synthesis and device fabrication of Bi_2Se_3 nanoribbons were reported previously,[17,21,22] with details given in the Experimental Section. Four-probe magnetoresistance, R_{xx} (Figure 1a), and Hall resistance, R_{xy} (Figure 1b), are measured by PPMS (Quantum Design), with a magnetic field applied perpendicular to the nanoribbon surfaces corresponding to the (0001) plane of Bi_2Se_3. SdH oscillations are observed both in R_{xx} and R_{xy}. The oscillation period, $(\Delta(1/B))^{-1}$, is determined as 86 T (Supporting Information). According to the band structure of Bi_2Se_3, SdH oscillations of the surface electrons are expected to have a

* Address correspondence to yicui@stanford.edu.

Received for review February 11, 2011 and accepted May 13, 2011.

Published online May 13, 2011
10.1021/nn200556h

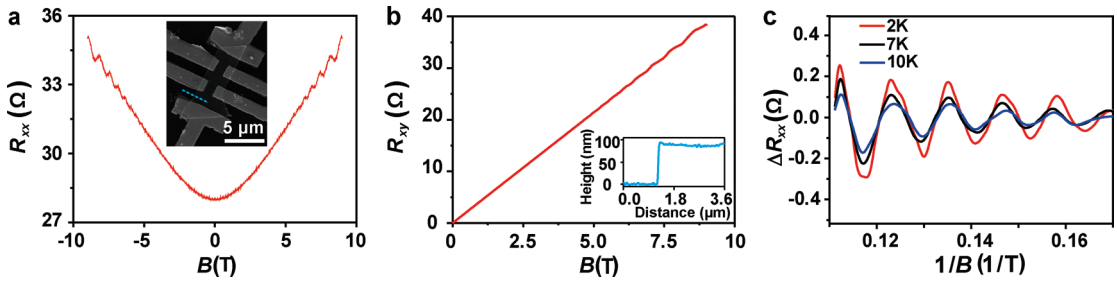

Figure 1. Transport measurements on Bi_2Se_3 nanoribbon device S1. (a) Magnetoresistance reveals pronounced SdH oscillations. Inset: SEM image of the device. (b) Hall resistance also shows SdH oscillations. Inset: AFM thickness profile corresponding to the line-cut of the SEM image in (a). (c) Temperature-dependent SdH oscillations in magnetoresistance after background subtraction.

much larger period when the Fermi level is near the bottom of the conduction band,[23] so we ascribe the observed oscillations to bulk electrons. In addition, cyclotron effective mass, $m^* = 0.13\ m_e$, obtained by fitting the thermal damping of the SdH oscillation amplitude (Figure 1c; details of the analyses are provided in the Supporting Information), is consistent with the value of bulk electrons from bulk single-crystal measurements.[20,24] For moderately doped samples ($n \lesssim 5 \times 10^{18}$ cm^{-3}), the Fermi surface of bulk states is approximately a prolate ellipsoid in momentum space.[24,25] Consequently, the SdH oscillation period should be proportional to $n_{3D}^{2/3}$ (see Supporting Information for derivation). Figure 2 shows previous bulk crystal SdH oscillation data fitted with this relation.[23,24,26] By fitting the curve, we estimate the bulk electron density in the nanoribbon as $n_{3D}^{SdH} = 4.7 \times 10^{18}$ cm^{-3} (Figure 2). On the other hand, effective areal electron concentration in the nanoribbon is $n_{2D}^{Hall} = 1.5 \times 10^{14}$ cm^{-2}, obtained from the Hall slope of 4.28 Ω/T (Figure 1b). Hence, bulk electron concentration is $n_{3D}^{Hall} \approx 1.7 \times 10^{19}$ cm^{-3}, as the nanoribbon has a thickness of 88 nm measured by atomic force microscopy (AFM, Figure 1b inset). Apparently, n_{3D}^{Hall} is much higher than n_{3D}^{SdH}, indicating the existence of low mobility carriers inside the nanoribbon. The "discrepancy" between n_{3D}^{Hall} and n_{3D}^{SdH} is because these low-mobility carriers will not take part in the SdH oscillations, while present in the Hall measurements. We note that the TI SS is not expected to be the dominant source of the additional carriers owing to the relatively low density of 2D electronic states. Transport measurements on bulk single crystals typically show consistency between the carrier concentration estimated by the Hall slope and SdH oscillation period.[18,20] A few bulk crystal experiments reveal lower carrier concentration from the Hall slope compared to that from the SdH oscillation,[24] which is expected for the Hall measurement on a multicarrier material at low field limit. The large Hall carrier concentration n_{3D}^{Hall} with a factor of ~3.6 larger than n_{3D}^{SdH} observed in our Bi_2Se_3 nanoribbon is rarely seen in bulk crystals. It was reported previously that excessive electrons accumulate on the surface of Bi_2Se_3 crystals over time.[18,20] In a lightly doped Bi_2Se_3 bulk crystal ($n \approx 10^{17}$ cm^{-3}), the Fermi energy at the surface acquired by ARPES increases to a degenerate level upon exposure to air, which corresponds to the accumulation of electrons that bend the bulk band near the crystal surface.[20] In addition, time-dependent transport studies on lightly doped bulk crystals exposed to humid atmosphere reveal the continuous n-type doping from the environment.[18] For the nanoribbon case, the environmentally doped electrons contribute to the transport with a much more pronounced effect due to the large surface-to-volume ratio in nanostructures. It is therefore reasonable to ascribe the excessive electrons revealed in the Hall measurement to environmentally doped carriers, possibly with low mobility, that do not contribute to the SdH oscillations.

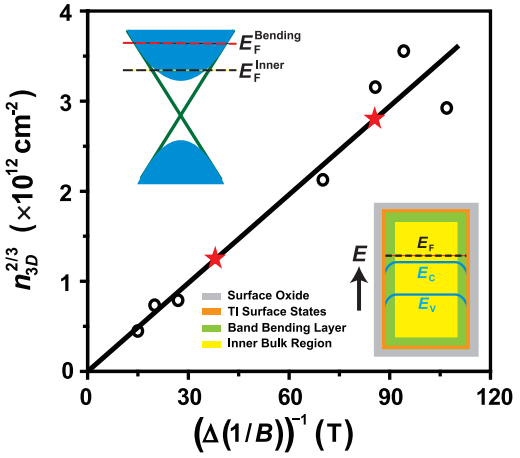

Figure 2. Plot of $n_{3D}^{2/3}$ versus $(\Delta(1/B))^{-1}$ fitted with a linear relation. Open circles are data collected from previous measurements on bulk single crystals.[23,24,26] Carrier concentration of the nanoribbon device is thus obtained, as marked by the red stars. Upper inset: Schematic band structure of Bi_2Se_3, with different Fermi levels for environmentally doped layer (red) and crystal inner region (black). Lower inset: Structure of Bi_2Se_3 nanoribbons consisting of a surface oxide layer, topological insulator surface states, a heavily doped layer from environmental doping (low mobility), and a moderately doped inner region (high mobility). Diagram of Fermi level, conduction, and valence band edges through the nanoribbon is also shown. The existence of surface oxide is revealed by XPS characterizations (shown in Figure 3).

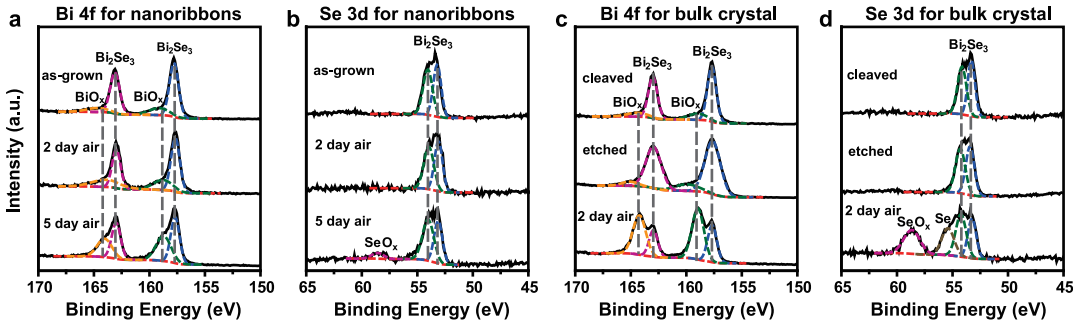

Figure 3. XPS studies on Bi_2Se_3 nanoribbons with Bi 4f (a) and Se 3d (b) spectra, including samples after synthesis, aged in air for 2 days, and aged for 5 days. XPS studies on a Bi_2Se_3 single crystal with Bi 4f (c) and Se 3d (d) spectra, including samples right after cleaving (<10 s air exposure), etched with Ar plasma for 5 min, and aged in air for 2 days. The observed surface oxide may exist in hydroxide form, which is difficult to distinguish from oxide due to the broadness of the oxide peak.

To examine the physical origin of the environmental doping on Bi_2Se_3, surface chemistry probe XPS (SSI S-Probe XPS spectrometer with Al Ka source) is used to characterize the composition at the surface of Bi_2Se_3 nanoribbons and bulk single crystals. Silicon substrates with full coverage of nanoribbons are selected for XPS study to avoid the substrate contribution in the final spectra. For as-grown nanoribbons (Figure 3a and b), a bismuth oxide (BiO_x) peak is observed.[27] Here, we cannot exclude the possibility that the observed surface oxide exists in the hydroxide form, which is difficult to distinguish from the oxide due to the broadness of the oxide peak overlapping the energy range of the hydroxide. We note that previous energy dispersive X-ray spectroscopy (EDS) characterizations on Bi_2Se_3 nanoribbons, performed in a transmission electron microscope (TEM), reveal negligible oxygen content with respect to the bismuth and Se.[17,21,22] XPS is a surface-sensitive technique, whereas TEM-EDS probes the compositions of the whole nanoribbon since the electron beam transmits through the sample. Comparison between XPS and EDS analyses indicates the oxide is formed on the surface of the nanoribbons. Time evolution of the surface oxide is studied with nanoribbons stored in air (Figure 3a and b). As the air exposure time increases, the BiO_x peak keeps growing, corresponding to the increase of BiO_x thickness. For nanoribbons exposed in air for 5 days, selenium oxide (SeO_x) is also observed (Figure 3b). The absence of SeO_x for samples with relatively short time exposure to air may come from the stronger tendency of O_2 to react with Bi or the high vapor pressure of Se. The thickness of the surface oxide is difficult to estimate due to the random orientations of the nanoribbons. We also performed an XPS study on bulk single crystals of Bi_2Se_3 with low carrier concentrations. These crystals are grown with similar methods to those in ref 23 (details also provided in Experimental Section), on which the environmental doping effects are revealed by ARPES measurements. Fresh surfaces are readily available by cleaving the crystals along their natural cleavage plane, which allows us to investigate the time scale of the oxide formation. To minimize ambient exposure, the Bi_2Se_3 crystal is loaded into the XPS sample chamber right after cleaving (within 10 s) and pumped down to vacuum with high-purity N_2 gas flux. The BiO_x signal is clearly observed in the final spectra (Figure 3c and d), which indicates the formation of the "native" oxide is very fast. The thickness of the surface oxide is estimated as ~0.38 nm, by assuming a bilayer structure with BiO_x on top and Bi_2Se_3 underneath (Experimental Section). The oxide peak can be reduced by a short argon (Ar) ion etching for 5 min (10 mA, 5 kV); the weight of the BiO_x peak decreases from 19% to 13% after Ar etch, further confirming the surface origin of the oxide. Spectra of the cleaved bulk crystal with longer air aging of 2 days are also acquired, revealing a dramatically increased BiO_x peak. The SeO_x peak is also observed in such long time aged samples, similar to the nanoribbon case. The surface oxide thickness of 2-day air-exposed samples is estimated as ~1.94 nm (Experimental Section). Interestingly, the elemental Se peak is also present in the same spectra. A tentative explanation is that some Se in the Bi_2Se_3 crystal grown with excessive Se powder tends to gradually precipitate out, since a Se-deficient state is more thermodynamically favorable under ambient conditions.

The growth of native oxide (or hydroxide) on Bi_2Se_3 nanoribbons and bulk crystals may account for many challenges in transport measurements of TIs. Environmental doping from surface oxide growth is known for many semiconductors, such as germanium (Ge) and gallium nitride (GaN):[28,29] Semiconductor bulk bands bend near the oxide/semiconductor interface. It may directly come from the induced charges in the semiconductor from the trapped charges in the oxide or at the semiconductor/oxide interface,[29,30] or the formation of interfacial defect states giving rise to the Fermi level pinning at the interface and bulk bands bending.[28] We note that surface oxidation involving only oxygen is a p-type doping process for Bi_2Se_3.[16] Moisture-assisted surface oxidation of Bi_2Se_3 in air may exhibit distinctive interfacial defects or trapped charges different from the pure oxygen case, which results in the reversed doping

effect. Another possibility is an indirect mechanism. The surface oxide is expected to be decorated with hydroxyl groups as surface impurities under ambient conditions, especially at defect sites.[31] Hydroxyl impurities are typically electron donors that lead to n-type band bending.[32] The dominant contributor to the n-type surface doping for Bi_2Se_3 requires further study. For continuous surface oxide growth, oxygen atoms need to diffuse into the crystal and locally distort the perfect layered crystal structure, increasing disorder on the surface. Furthermore, continuous surface oxide growth is also observed in bismuth telluride (Bi_2Te_3),[33] another layered TI with a structure close to that of Bi_2Se_3.[6,34] Such surface oxidation appears to be general for this family of TIs. The current study does not exclude alternative mechanisms contributing to the environmental doping and surface degradation process. For example, absorbed water (H_2O) serves as an electron donor for certain layered chalcogenide semiconductors, even without appreciable surface reactions.[35] The aging of the Bi_2Se_3 surface in the atmosphere is likely the collective effect from multiple factors.

We can qualitatively evaluate the transport properties of the Bi_2Se_3 nanoribbons. The conductance of the nanoribbon comes from parallel contributions from the environmentally doped band bending region, nondoped inner region, and TI SS (schematic shown in Figure 2). The doped region is expected as a thin layer encapsulating the nanoribbon, due to the strong screening in metallic Bi_2Se_3. Topological SS exist at the interface between the doped layer and surface oxide. The effective Hall mobility of the nanoribbon μ_H is 630 $cm^2/(V\ s)$, determined by the measured Hall slope of 4.28 Ω/T and the sheet resistance of 68 Ω. The Hall mobility is the averaged mobility of different types of carriers. The mobility of the nondoped inner bulk region is extracted from thermal damping of the amplitude of the SdH oscillations (details in the Supporting Information). The isotropic scattering time for inner bulk electrons, $\tau_{iso,3D}$, is 0.08 ps, corresponding to a mobility, $\mu_{iso,3D}$, of 1100 $cm^2/(V\ s)$. The conductance of the inner region is determined by the transport mobility, $\mu_{t,3D}$, which is larger than $\mu_{iso,3D}$ for a 3D electron gas. The ratio of $\mu_{t,3D}/\mu_{iso,3D}$ varies depending on microscopic scattering processes.[24,36] Recent measurements on bulk single crystals show the ratio can be as large as 4.[24] Therefore, $\mu_{t,3D}$ is expected to be a few thousand $cm^2/(V\ s)$. A comparison between μ_H and $\mu_{t,3D}$ indeed reveals that a significant amount of low-mobility carriers exist in the nanoribbon. The major source of such low-mobility electrons is from the doped band bending region, since it holds the largest population of the carriers. The decrease of the mobility in the band bending layer is ascribed to the addition of interface defects during oxide growth. The mobility of topological SS may vary with the surface condition. In bulk Bi_2Se_3 crystals with minimal air exposure, SdH oscillations of SS are observed in pulse field measurements, with a relatively high isotropic scattering mobility of 1750 $cm^2/(V\ s)$. Nevertheless, the environmental doping as well as the increase of surface scattering, associated with the oxidation process, adds challenges in probing topological SS. As shown in Figure 2, environmental doping induces band bending at the Bi_2Se_3 surface and shifts the Fermi level deeper into the conduction band. Under extreme cases, the topological SS may merge into the bulk conduction band and become nondistinguishable from bulk states in transport measurements. In addition, even though TI SS are protected by the time reversal symmetry and are insensitive to a backscattering process, they are not completely immune to other scattering routes. The increase of surface disorders therefore would still lower SS mobility. The smearing of SS SdH oscillations of Bi_2Se_3 after 1−2 h air exposure[18] and the absence of surface transport signature in high-quality single crystals reveal such a degradation process of topological SS transport properties after Bi_2Se_3 interaction with the ambient environment. Certainly, these results implore extreme caution in handling Bi_2Se_3 samples, to minimize the extraneous SS degradation effects from atmosphere exposure. The extent of the surface chemical reactions and their influence on the transport properties of TI SS may depend on the sample quality or growth conditions. This study does not exclude the opportunity to obtain Bi_2Se_3 crystals with relatively robust surface transport properties under ambient conditions.

CONCLUSION

In summary, the observed discrepancy between the Hall- and SdH-estimated carrier concentrations in Bi_2Se_3 nanoribbons indicates n-type doping by air exposure, consistent with previous measurements on bulk single crystals. XPS characterizations on Bi_2Se_3 nanoribbons and bulk single crystals reveal the rapid formation and continuous growth of surface oxide under ambient conditions. This oxide growth may serve as the physical origin of surface degradation and environmental doping on Bi_2Se_3. It presents a practical challenge for probing TI SS by transport measurements. Appropriate encapsulation or surface passivation to inhibit the surface oxidation may be required.

EXPERIMENTAL SECTION

Bi_2Se_3 Nanoribbon Synthesis and Device Fabrication. Bi_2Se_3 nanoribbons are synthesized by metal-catalyzed vapor phase growth in a horizontal tube furnace.[17,23,24] As-grown Bi_2Se_3 nanoribbons are grown by using 20 nm gold nanoparticles as catalyst. Sn-doped Bi_2Se_3 nanoribbons are grown with Sn/Au (5 nm/2 nm)

double-layer alloy catalysts, where the dopant is introduced by the diffusion from the catalyst during the growth. Nanoribbons exhibit a well-defined structure, with very smooth top and bottom surfaces perpendicular to the (0 0 0 1) trigonal axis. The synthesis is based on a combined vapor−liquid−solid (VLS) and vapor−solid (VS) mechanism, in which the VLS process promotes one-dimensional growth from the metal catalyst, and the VS process favors direct deposition on the side surface of the nanoribbon for two-dimensional growth. The involvement of the VS process for the growth of wide nanoribbons is supported by the catalyst-free growth of Bi_2Se_3 nanoplates with conditions close to the nanoribbon synthesis.[37] As-grown Bi_2Se_3 nanoribbons using gold particles have a higher yield than Sn-doped Bi_2Se_3 nanoribbons. Hence we used gold-catalyzed nanoribbons, which can completely cover a substrate, for XPS measurements, to improve the signal-to-noise ratio and avoid contributions from the substrate. Sn-doped nanoribbons are selected for transport study. Sn effectively compensates residue bulk electrons induced from Se vacancies and improves the transport mobility,[17] allowing us to observe Aharonov−Bohm oscillations reported previously and Shubnikov−de Haas oscillations discussed here. Sn-doped nanoribbons still remain metallic. EDS characterizations on Sn-doped nanoribbons reveal little signal of Sn within the detection limit (∼1−2%). Typically, only a trace amount of the dopant is introduced to the nanostructures by diffusion from the catalyst.[38] Therefore, Sn-doped nanoribbons are expected to exhibit similar surface chemical properties to as-grown nanoribbons with a relatively low concentration of Sn dopants.

Bi_2Se_3 nanoribbons are mechanically transferred from the growth substrate onto a 150 nm thick silicon nitride on Si substrate. Titanium (Ti)/Au (5 nm/195 nm) or chromium (Cr)/Au (5 nm/195 nm) ohmic contacts are patterned on nanoribbons to form six-terminal configurations, through standard e-beam lithography followed by thermal evaporation of the metals.

Bi_2Se_3 Bulk Single Crystal Growth. Single crystals of Bi_2Se_3 have been grown by slow cooling a binary melt. Elemental Bi and Se are mixed in alumina crucibles in a molar ratio of 35:65. The mixtures are sealed in quartz ampules, raised to 750 °C, cooled slowly to 550 °C, and then annealed for an extended period. Crystals grown with such nominal composition ratio containing excessive Se exhibit reduced defect density and low carrier concentration.[20]

Transport Measurements. Standard low-frequency (1000 Hz) four-probe magnetoresistance measurements are carried out in a Quantum Design PPMS-7 instrument, Janis-9T magnet Hecryostats, and a Keithley S110 Hall effect measurement system. The temperature range is 2−300 K, and the magnetic field is up to ±9 T. The field is applied to the normal direction of the nanoribbon surfaces, corresponding to the (0001) plane of Bi_2Se_3.

XPS Sample Preparation and Surface Oxide Thickness Estimation. XPS characterizations on nanoribbons are performed directly on as-grown substrates. High-yield substrates with full coverage of the nanoribbons are selected, to eliminate the contribution from the substrates to the final spectra. The flat surface of Bi_2Se_3 bulk single crystals is available by cleaving the crystal along its natural cleavage plane (perpendicular to its trigonal axis).

To estimate the thickness of the oxide, we assume a bilayer structure with the surface oxide on top and Bi_2Se_3 underneath. We obtain the atomic concentration of Bi_2Se_3:BiO_x as 81.4%:18.7%, from areas under the Bi_2Se_3 and BiO_x peak in Bi^{4f} transitions. Using the electron escape depth of 1.8 nm (typical for Al Ka source), the attenuation of the Bi_2Se_3 peak from 100% to 81.4% due to the surface oxide gives the oxide thickness of ∼0.38 nm for samples with minimum air exposure. After 5 min etching, the BiO_x peak is reduced to 13%. We note that it is difficult to accurately estimate the amount of remaining BiO_x after etching since the Bi peak widens. For crystals aged in air for 2 days, we observe an increased BiO_x peak as well as SeO_x peak. Assuming again the bilayer structure with surface oxide on top and Bi_2Se_3 underneath, the attenuation of the Bi_2Se_3 peak from 100% to 34.1% gives the surface oxide thickness of ∼1.94 nm for a 2-day-exposed sample.

Acknowledgment. Y.C. acknowledges the supported from the Keck Foundation and King Abdullah University of Science and Technology (KAUST) Investigator Award (No. KUS-I1-001-12). K.L. acknowledges the KAUST Postdoctoral Fellowship support No. KUS-F1-033-02. J.G.A. and I.R.F. acknowledge support from the Department of Energy, Office of Basic Energy Sciences, under contract DE-AC02-76SF00515.

Supporting Information Available: EDS spectrum of Sn-doped nanribbons of Bi_2Se_3 and details on the analyses of SdH oscillations. This material is available free of charge *via* the Internet at http://pubs.acs.org.

REFERENCES AND NOTES

1. Moore, J. E. The Birth of Topological Insulators. *Nature* **2010**, *464*, 194–198.
2. Hasan, M. Z.; Kane, C. L. Colloquium: Topological Insulators. *Rev. Mod. Phys.* **2010**, *82*, 3045.
3. Qi, X.-L.; Zhang, S.-C. Topological Insulators and Superconductors. Preprint avaible at http://arxiv.org/abs/1008.2026.
4. Fu, L.; Kane, C. L. Topological Insulators with Inversion Symmetry. *Phys. Rev. B* **2007**, *76*, 045302.
5. Zhang, H.-J.; Liu, C.-X.; Qi, X.-L.; Deng, X.-Y.; Dai, X.; Zhang, S.-C.; Fang, Z. Electronic Structures and Surface States of the Topological Insulator $Bi_{1-x}Sb_x$. *Phys. Rev. B* **2009**, *80*, 085307.
6. Zhang, H.; Liu, C.-X.; Qi, X.-L.; Dai, X.; Fang, Z.; Zhang, S.-C. Topological Insulators in Bi_2Se_3, Bi_2Te_3 and Sb_2Te_3 with a Single Dirac Cone on the Surface. *Nat. Phys.* **2009**, *5*, 438–442.
7. Xia, Y.; Qian, D.; Hsieh, D.; Wray, L.; Pal, A.; Lin, H.; Bansil, A.; Grauer, D.; Hor, Y. S.; Cava, R. J.; *et al.* Observation of a Large-Gap Topological-Insulator Class with a Single Dirac Cone on the Surface. *Nat. Phys.* **2009**, *5*, 398–402.
8. Yan, B.; Liu, C.-X.; Zhang, H.-J.; Yam, C.-Y.; Qi, X.-L.; Frauenheim, T.; Zhang, S.-C. Theoretical Prediction of Topological Insulators in Thallium-Based III-V-VI_2 Ternary Chalcogenides. *EPL* **2010**, *90*, 37002.
9. Lin, H.; Markiewicz, R. S.; Wray, L. A.; Fu, L.; Hasan, M. Z.; Bansil, A. Single-Dirac-Cone Topological Surface States in the $TlBiSe_2$ Class of Topological Semiconductors. *Phys. Rev. Lett.* **2010**, *105*, 036404.
10. Chadov, S.; Qi, X.; Kübler, J.; Fecher, G. H.; Felser, C.; Zhang, S. C. Tunable Multifunctional Topological Insulators in Ternary Heusler Compounds. *Nat. Mater.* **2010**, *9*, 541–545.
11. Lin, H.; Wray, L. A.; Xia, Y.; Xu, S.; Jia, S.; Cava, R. J.; Bansil, A.; Hasan, M. Z. Half-Heusler Ternary Compounds as New Multifunctional Experimental Platforms for Topological Quantum Phenomena. *Nat. Mater.* **2010**, *9*, 546–549.
12. Xu, S.-Y.; Wray, L. A.; Xia, Y.; Shankar, R.; Petersen, A.; Fedorov, A.; Lin, H.; Bansil, A.; Hor, Y. S.; Grauer, D.;*et al.* Discovery of Several Large Families of Topological Insulator Classes with Backscattering-Suppressed Spin-Polarized Single-Dirac-Cone on the Surface. Preprint avaible at http://arxiv.org/abs/1007.5111.
13. Hsieh, D.; Xia, Y.; Qian, D.; Wray, L.; Dil, J. H.; Meier, F.; Osterwalder, J.; Patthey, L.; Checkelsky, J. G.; Ong, N. P.; *et al.* A Tunable Topological Insulator in the Spin Helical Dirac Transport Regime. *Nature* **2009**, *460*, 1101–1105.
14. Zhang, Y.; He, K.; Chang, C.-Z.; Song, C.-L.; Wang, L.-L.; Chen, X.; Jia, J.-F.; Fang, Z.; Dai, X.; Shan, W.-Y.; *et al.* Crossover of the Three-Dimensional Topological Insulator Bi_2Se_3 to the Two-Dimensional Limit. *Nat. Phys.* **2010**, *6*, 584–588.
15. Wray, L. A.; Xu, S.-Y.; Xia, Y.; Hor, Y. S.; Qian, D.; Fedorov, A. V.; Lin, H.; Bansil, A.; Cava, R. J.; Hasan, M. Z. Observation of Topological Order in a Superconducting Doped Topological Insulator. *Nat. Phys.* **2010**, *6*, 855–859.
16. Chen, Y. L.; Chu, J.-H.; Analytis, J. G.; Liu, Z. K.; Igarashi, K.; Kuo, H.-H.; Qi, X. L.; Mo, S. K.; Moore, R. G.; Lu, D. H.; *et al.* Massive Dirac Fermion on the Surface of a Magnetically Doped Topological Insulator. *Science* **2010**, *329*, 659–662.
17. Peng, H.; Lai, K.; Kong, D.; Meister, S.; Chen, Y.; Qi, X.-L.; Zhang, S.-C.; Shen, Z.-X.; Cui, Y. Aharonov-Bohm

Interference in Topological Insulator Nanoribbons. *Nat. Mater.* **2010**, *9*, 225–229.
18. Analytis, J. G.; McDonald, R. D.; Riggs, S. C.; Chu, J.-H.; Boebinger, G. S.; Fisher, I. R. Two-Dimensional Surface State in the Quantum Limit of a Topological Insulator. *Nat. Phys.* **2010**, *6*, 960–964.
19. Sacepe, B.; Oostinga, J. B.; Li, J.; Ubaldini, A.; Couto, N. J. G.; Giannini, E.; Morpurgo, A. F. Gate-Tuned Normal and Superconducting Transport at the Surface of a Topological Insulator. Preprint avaible at http://arxiv.org/abs/1101.2352.
20. Analytis, J. G.; Chu, J.-H.; Chen, Y.; Corredor, F.; McDonald, R. D.; Shen, Z. X.; Fisher, I. R. Bulk Fermi Surface Coexistence with Dirac Surface State in Bi_2Se_3: A Comparison of Photoemission and Shubnikov-De Haas Measurements. *Phys. Rev. B* **2010**, *81*, 205407.
21. Kong, D.; Randel, J. C.; Peng, H.; Cha, J. J.; Meister, S.; Lai, K.; Chen, Y.; Shen, Z.-X.; Manoharan, H. C.; Cui, Y. Topological Insulator Nanowires and Nanoribbons. *Nano Lett.* **2010**, *10*, 329–333.
22. Cha, J. J.; Williams, J. R.; Kong, D.; Meister, S.; Peng, H.; Bestwick, A. J.; Gallagher, P.; Goldhaber-Gordon, D.; Cui, Y. Magnetic Doping and Kondo Effect in Bi_2Se_3 Nanoribbons. *Nano Lett.* **2010**, *10*, 1076–1081.
23. Butch, N. P.; Kirshenbaum, K.; Syers, P.; Sushkov, A. B.; Jenkins, G. S.; Drew, H. D.; Paglione, J. Strong Surface Scattering in Ultrahigh-Mobility Bi_2Se_3 Topological Insulator Crystals. *Phys. Rev. B* **2010**, *81*, 241301(R).
24. Eto, K.; Ren, Z.; Taskin, A. A.; Segawa, K.; Ando, Y. Angular-Dependent Oscillations of the Magnetoresistance in Bi_2Se_3 Due to the Three-Dimensional Bulk Fermi Surface. *Phys. Rev. B* **2010**, *81*, 195309.
25. Köhler, H. Conduction Band Parameters of Bi_2Se_3 from Shubnikov-de Haas Investigations. *Phys. Status Solidi B* **1973**, *58*, 91–100.
26. Kulbachinskii, V. A.; Miura, N.; Nakagawa, H.; Arimoto, H.; Ikaida, T.; Lostak, P.; Drasar, C. Conduction-Band Structure of $Bi_{2-x}Sb_xSe_3$ Mixed Crystals by Shubnikov-de Haas and Cyclotron Resonance Measurements in High Magnetic Fields. *Phys. Rev. B* **1999**, *59*, 15733.
27. Dharmadhikari, V. S.; Sainkar, S. R.; Badrinarayan, S.; Goswami, A. Characterisation of Thin Films of Bismuth Oxide by X-Ray Photoelectron Spectroscopy. *J. Electron Spectrosc. Relat. Phenom.* **1982**, *25*, 181–189.
28. Wang, D.; Chang, Y.-L.; Wang, Q.; Cao, J.; Farmer, D. B.; Gordon, R. G.; Dai, H. Surface Chemistry and Electrical Properties of Germanium Nanowires. *J. Am. Chem. Soc.* **2004**, *126*, 11602–11611.
29. Garcia, M. A.; Wolter, S. D.; Kim, T. H.; Choi, S.; Baier, J.; Brown, A.; Losurdo, M.; Bruno, G. Surface Oxide Relationships to Band Bending in GaN. *Appl. Phys. Lett.* **2006**, *88*, 013506.
30. Goetzberger, A.; Heine, V.; Nicollian, E. H. Surface States in Silicon from Charges in the Oxide Coating. *Appl. Phys. Lett.* **1968**, *12*, 95–97.
31. Al-Abadleh, H. A.; Grassian, V. H. Oxide Surfaces as Environmental Interfaces. *Surf. Sci. Rep.* **2003**, *52*, 63–161.
32. Minato, T.; Sainoo, Y.; Kim, Y.; Kato, H. S.; Aika, K.-i.; Kawai, M.; Zhao, J.; Petek, H.; Huang, T.; He, W.; *et al.* The Electronic Structure of Oxygen Atom Vacancy and Hydroxyl Impurity Defects on Titanium Dioxide (110) Surface. *J. Chem. Phys.* **2009**, *130*, 124502.
33. Bando, H.; Koizumi, K.; Oikawa, Y.; Daikohara, K.; Kulbachinskii, V. A.; Ozaki, H. The Time-Dependent Process of Oxidation of the Surface of Bi_2Te_3 Studied by X-Ray Photoelectron Spectroscopy. *J. Phys.: Condens. Matter* **2000**, *12*, 5607–5616.
34. Chen, Y. L.; Analytis, J. G.; Chu, J.-H.; Liu, Z. K.; Mo, S.-K.; Qi, X. L.; Zhang, H. J.; Lu, D. H.; Dai, X.; Fang, Z.; *et al.* Experimental Realization of a Three-Dimensional Topological Insulator, Bi_2Te_3. *Science* **2009**, *325*, 178–181.
35. Mayer, T.; Klein, A.; Lang, O.; Pettenkofer, C.; Jaegermann, W. H_2O Adsorption on the Layered Chalcogenide Semiconductors WSe_2, InSe and GaSe. *Surf. Sci.* **1992**, *269/270*, 909–914.
36. Das Sarma, S.; Stern, F. Single-Particle Relaxation Time Versus Scattering Time in an Impure Electron Gas. *Phys. Rev. B* **1985**, *32*, 8442–8444.
37. Kong, D.; Dang, W.; Cha, J. J.; Li, H.; Meister, S.; Peng, H.; Liu, Z.; Cui, Y. Few-Layer Nanoplates of Bi_2Se_3 and Bi_2Te_3 with Highly Tunable Chemical Potential. *Nano Lett.* **2010**, *10*, 2245–2250.
38. Allen, J. E.; Hemesath, E. R.; Perea, D. E.; Lensch-Falk, J. L.; Li, Z. Y.; Yin, F.; Gass, M. H.; Wang, P.; Bleloch, A. L.; Palmer, R. E.; *et al.* High-Resolution Detection of Au Catalyst Atoms in Si Nanowires. *Nat. Nanotechnol.* **2008**, *3*, 168–173.